



Improved potential energy surfaces of thioanisole and the effect of upper surface variations on the product distribution upon photodissociation[☆]

Yinan Shu, Donald G. Truhlar*

Department of Chemistry, Chemical Theory Center, and Minnesota Supercomputing Institute, University of Minnesota, Minneapolis, MN 55455-0431, USA

ABSTRACT

Electronically nonadiabatic photodissociation can be investigated in detail by experiments. This provides an opportunity to validate the current theory of electronically nonadiabatic processes, but is great challenge because the time scale of photodissociation processes can be long compared to the current capability for accurate direct dynamics simulations. To circumvent this difficulty, we have been using analytic diabatic potential energy matrices, such that the simulation time scale can be extended to the nanosecond region without neglecting the effects of external electron correlation. In previous work, we have developed full-dimensional three-state potential energy matrices for thioanisole photodissociation. In the current work, we extend this work in two main ways: (i) we improve the treatment of the initial torsional potential, and (ii) we shift the potential energy surfaces to investigate the quantitative effect on the dissociation lifetimes and product branching ratios of changing the energy and location of the S_1 – S_2 conical intersection.

1. Introduction

Accurate simulations of photochemical and photophysical processes, such as vision, photosynthesis, and photocatalysis, are among the most challenging problems in theoretical chemistry. Photodissociation is an important class of nonadiabatic molecular processes that has been studied in detail by both experiments and theoretical simulations [1–31]. Because dynamics in electronically excited states is typically electronically nonadiabatic, one must consider non-Born-Oppenheimer effects in the simulations [32–42].

The subject of the present paper is the photodissociation of thioanisole. Figure 1 shows a schematic cut through the potential energy surfaces for the three lowest singlet states. In the photodissociation process considered here, the molecule is photo-excited to S_1 , it converts to S_2 in the vicinity of the first conical intersection seam (CI1), and then it dissociates, passing the second conical intersection seam (CI2), at which point the flux branches between dissociation to the ground doublet states of both radicals, PhS[D_0] + CH₃[D_0], or to excited thiophenoxy radical plus ground-state methyl, PhS[D_1] + CH₃[D_0] [22]. The experiments yielded a lifetime of the thioanisole photodissociation process of about 1–2 ns [43,44]. In addition, the experiments showed that the D_0/D_1 product branching ratio increases smoothly from 0.05 for excitation of the ground state of S_1 to a plateau of about 0.17 as the vibrational energy is increased, except for a

dramatic spike up to 0.42 when the S-CH₃ vibrational mode is excited. Explaining this mode-specific enhancement is a challenge for theory.

Motivated by these results, our group has recently developed [45] full-dimensional three-state diabatic potential energy matrices (PEMs) of thioanisole based on the anchor points reactive potential [46] (APRP) method. Each matrix element of a diabatic PEM is a function of the internal coordinates; the diagonal elements of the PEM are diabatic potential energy surfaces (PESs), and the off-diagonal elements are scalar diabatic couplings. Diagonalization of the PEM yields the adiabatic PESs as eigenvalues, and the vector surface couplings in the adiabatic representation (usually called nonadiabatic couplings or NACs) may be approximated from the eigenvectors. The coupled surfaces were used for multi-surface trajectory simulations by the coherent switches with decay of mixing algorithm, and the results showed final translational energy distributions similar to the experimental results, but with too short a lifetime (0.3 ps) and too high a D_0/D_1 product branching ratio (0.45–0.46), and without exhibiting the S-CH₃ vibrational mode selectivity [30].

In the present work, we have improved the three-state full dimensional APRP PEMs of thioanisole in three respects: (1) The dependence of the ground-state adiabatic potential energy surface (PES) on the torsional angle between the CH₃ group and C₆H₅S group has been made more accurate based on density functional theory calculations. (2) The diabatic coupling matrix elements are made to decay to zero at the

[☆] This article is part of the Wolfgang Domcke 70th Birthday Festschrift in Chemical Physics.

* Corresponding author.

E-mail address: truhlar@umn.edu (D.G. Truhlar).

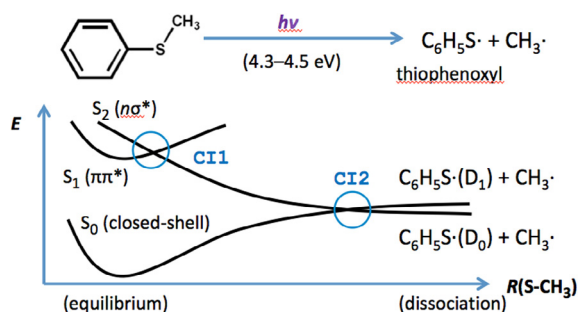


Fig. 1. Schematic potential energy curves for a cut through the thioanisole potential energy surfaces.

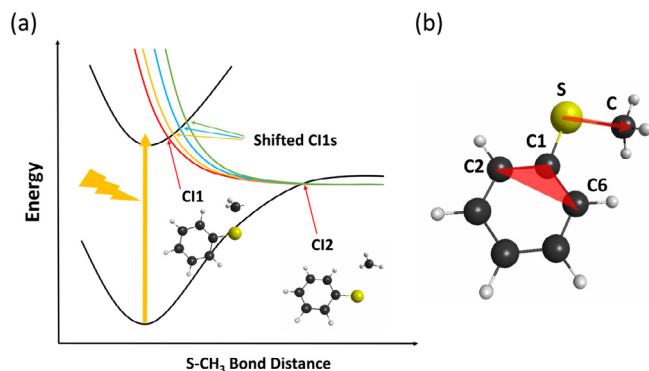


Fig. 2. (a) The schematic representation of the adiabatic PESs of thioanisole along the S-CH₃ bond distance and the shifted CIs, (b) the labeling of the atoms.

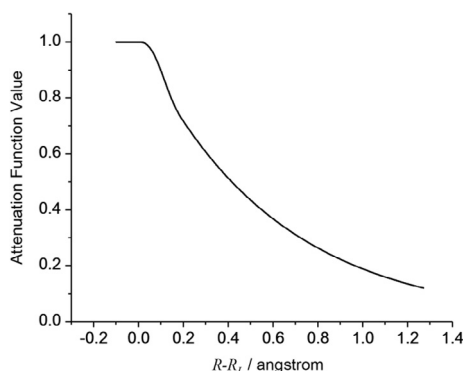


Fig. 3. The attenuation curve of Eq. (1).

dissociation limit by including an exponential decay function after the last anchor point along the S-CH₃ bond (an anchor point is a geometry selected as a fitting center in the APRP method). (3) The parameters in the analytic function for the PES of the third diabatic state are re-fitted to obtain a more accurate description at geometries with zero torsional angle. In addition to these improvements, we investigate the effect on the dynamics of the shifting the position and energy of the S₁–S₂ conical intersections.

The APRP fitting is done in the diabatic representation [47,48]. Hence, the shifting of the conical intersections CIs is achieved by shifting the analytical functions of the diabatic states. Fig. 2(a) is a schematic figure illustrating the shifts, and Fig. 2(b) shows the labeling of the atoms that is used throughout the text. Two primary coordinates will play a major role in the fitting: the S–CH₃ bond dissociation coordinate R and the torsional angle ϕ defined [45] as the angle between the S–C vector and the C₆–C₁–C₂ plane. When all geometrical parameters except these two primary coordinates are fixed at the ground-state equilibrium geometry, we shall refer to that as an equilibrium

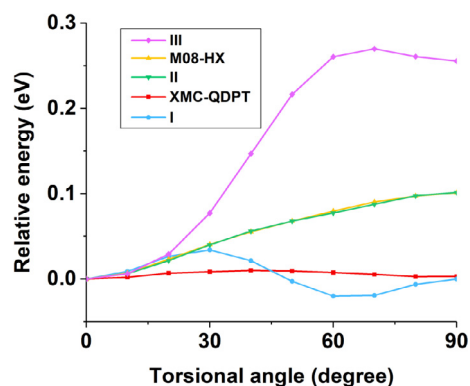


Fig. 4. The adiabatic ground-state torsional PESs of thioanisole computed by XMC-QDPT and I, KS/M08-HX and as yielded by PEMs I (same as Ia for these results), II, and III methods, represented as red, yellow, blue, green, and purple respectively. The yellow curve is hard to see because it is covered very well by the green curve. The results for surface Ia are the same as for surface I. (For interpretation of the references to colour in this figure legend, the reader is referred to the web version of this article.)

framework. (The equilibrium values of the S–C bond length R and the torsion angle ϕ are 1.82748 Å and 0° respectively.)

A key point in the thioanisole diabatization is that as ϕ is varied from 0 (corresponding – for C₂, C₁, C₆, and S being in the same plane – to C also being in that plane) to 90° (corresponding to S–C perpendicular to that plane), the ground adiabatic state S₀ changes from being dominated by diabatic state 1 to being dominated by diabatic state 3, i.e., diabatic states 1 and 3 undergo a crossing [49]. For this reason we improve diabatic state 3 in order to improve the S₀ torsional barrier.

2. The improved potential energy surfaces

The parameters of the APRP PEMs along the two primary coordinates were obtained [45] by fitting the 3 × 3 diabatic Hamiltonian matrix U as computed by the fourfold way transformation of the ab initio adiabatic surfaces V_i ($i = 1, 2, 3$ for S₀, S₁, and S₂); these adiabatic surfaces were obtained by extended multi-configurational quasi-degenerate second order perturbation theory (XMC-QDPT) [50–52], which adds external correlation onto CASSCF [53,54] results. The “fitted” adiabatic surfaces are not actually direct fits but rather obtained by diagonalizing the fitted U .

At the dissociation limit, the diabatic coupling matrix elements should be zero, but this was not the case in the originally published PEM [45], which is here called PEM I. This is corrected by multiplying all the off-diagonal diabatic Hamiltonian matrix elements (U_{12} , U_{13} , and U_{23} , by an attenuation function $f(R)$:

$$f(R) = \begin{cases} 1, & R < R_L \\ A(R-R_L)^5 + B(R-R_L)^4 + C(R-R_L)^3 + 1, & R_L \leq R \leq R_L + \Delta \\ e^{-D(R-R_L)}, & R > R_L + \Delta \end{cases} \quad (1)$$

where R_L is the S-CH₃ bond distance of the last anchor point [45], and A , B , C , D , and Δ are parameters. The middle spline function is employed to ensure that the attenuation function is smooth up to the second derivative. $R_L = 3.5$ Å, $A = -2951.3853314209523$ Å⁻⁵, $B = 1562.7687268060167$ Å⁻⁴, $C = -229.93090322936524$ Å⁻³. The attenuation curve is shown in Fig. 3. Correcting PEM I in this way yields a PEM called Ia. All the other PEMs are modifications of PEM Ia.

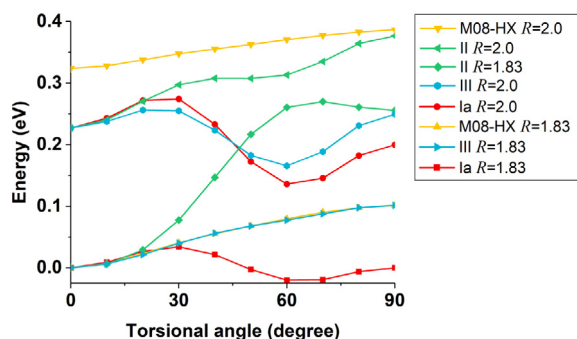
The XMC-QDPT calculations predict that the torsional potential along ϕ is very flat; it rises from 0 at 0° to 0.010 eV at 40° and then decreases to 0.003 eV at 90°; see the red curve in Fig. 4. Such a small torsional barrier makes the fitting very difficult because the flat adiabatic states are obtained by diagonalizing the directly fitted diabatic Hamiltonian with its rapidly varying and crossing state energies and

Table 1
Parameters of Eq. (2).

	I and Ia	II	III
$A_3/\text{hartree}$	-668.352732063236	-668.352732063236	-668.352732063236
$D_3/\text{hartree}$	1.65138486208663	4.025	4.025
$b_3/\text{\AA}^{-1}$	1.77311772459465	2.142	2.142
$B_3/\text{hartree}$	-0.05913514866085083	-0.06296612817531474	-0.06325301976068878
$\alpha/\text{\AA}^{-2}$	0.721710258187793	0.721710258187793	0.721710258187793
$R_3/\text{\AA}$	1.63756083461647	1.63756083461647	1.579
$C_3/\text{hartree}$	-0.03832768992221822	-0.04081069027402	-0.04099663538406905
$E_3/\text{hartree}$	0	0	-0.001
$\beta/\text{\AA}^{-2}$	0	0	1.2553141
$R_3/\text{\AA}$	0	0	1.82748

Table 2
Parameters of Eq. (3).

	I and Ia	II	III
$B_2^{(13)}/\text{hartree}$	-0.09737	-0.1003307	-0.097000229
$\alpha_2^{(13)}/\text{\AA}^{-2}$	0.848925978	0.848925978	0.848925978
$R_2^{(13)}/\text{\AA}$	1.507	1.507	1.507
$c_0^{(13)}/\text{hartree}$	-6.89806	-7.06718457	-7.39
$c_1^{(13)}/\text{hartree \AA}^{-1}$	3.90215	3.90215	3.90215
$\alpha_4^{(13)}/\text{\AA}^{-1}$	2.86681	2.86681	2.86681

**Fig. 5.** The torsional potentials for S-C distances of 1.83 and 2.0 Å. Notice that the yellow curve for the M08-HX potential with the S-C distance equal to 1.83 Å hard to see because it is behind the blue curve for PEM III for this S-C distance. (For interpretation of the references to colour in this figure legend, the reader is referred to the web version of this article.)**Table 3**

The energy levels and corresponding S-CH₃ internuclear distances of the optimized S₁-S₂ MECIs for the four shifted PEMs and surface III.

PEM	S ₁ -S ₂ MECI energy/eV	$\Delta V/\text{eV}^a$	S-CH ₃ bond distance/\AA	torsional angle/deg
S-1.8	4.59	0.23	1.98	0.0
III	4.65	0.29	2.01	0.0
S-2.0	4.68	0.32	2.02	0.0
S-2.2	4.78	0.42	2.06	0.0
S-2.5	4.90	0.54	2.10	0.0

^a $\Delta V = V(\text{S}_1\text{-S}_2 \text{ MECI}) - V(\text{S}_1 \text{ minimum})$.

large diabatic couplings. In the published fit [45], which in the present article is called PEM I, meV accuracy for this torsion was compromised to make other aspects of the fit accurate; the resulting fit, shown in blue in Fig. 4, is reasonably accurate but unfortunately has oscillatory behavior, which may be undesirable for quantal wave packet calculations.

The M08-HX [55] exchange-correlation functional has been well validated for energetics of toluene reactions [56], and we expect it should also be reasonably accurate for thioanisole; the torsional barrier

Table 4

The energy levels and corresponding S-CH₃ internuclear distances of the optimized S₀-S₁ MECIs for the four shifted PEMs and surface III.

PEM	S ₀ -S ₁ MECI energy/eV	S-CH ₃ bond distance/\AA	torsional angle/deg
S-1.8	2.92	3.26	0.0
III	2.87	3.26	0.0
S-2.0	2.92	3.26	0.0
S-2.2	2.93	3.26	0.0
S-2.5	2.95	3.27	0.0

Table 5

The lifetime and number of D₀ and D₁ trajectories^a for each of the initial conditions and PEMs employed in dynamics.^{a,b}

PEM	M0		M23					
	Lifetime/ps	D ₀	D ₁	D ₀ /D ₁	Lifetime/ps	D ₀	D ₁	D ₀ /D ₁
S-1.8	2.3	280	720	0.39	1.6	301	697	0.43
III	11.6	276	723	0.38	5.7	287	710	0.40
S-2.0	14.1	270	729	0.37	7.9	288	712	0.40
S-2.2	41.4	242	757	0.32	25.2	253	745	0.34
S-2.5	171.1	216	746	0.29	105.8	218	774	0.28

^a D₀ is the number of trajectories with dissociation products PhS[D₁] + CH₃[D₀], and D₁ is the number of trajectories with dissociation products PhS[D₀] + CH₃[D₀].

^b The average lifetime was computed as the average time for dissociative trajectories to reach 12 Å separation of S from C minus 0.2 ps, which is the average time of flight from 6 Å (which is a more reasonable estimate of the time at which the system may be considered dissociated) to 12 Å (where we actually stopped the trajectories).

predicted by this method is 0.101 eV at 90°. The yellow curve in Fig. 4 shows the ground-state adiabatic PES along the torsional coordinate as calculated by M08-HX; both the XMC-QDPT and M08-HX calculations were performed with the 6-311 + G(d) basis set [57,58] for carbon and hydrogen and the MG3S basis [59] for sulfur by using the GAMESS software [60,61]. The MG3S basis set is explained in previous publications [59,62,63]; for S, it differs from 6-311 + G(3d2f) by having an improved contraction scheme [62].

First we re-fit the diabatic Hamiltonian matrix elements along ϕ to reproduce the M08-HX adiabatic potential. This improved APRP PEM will be denoted as surface II, and it yields the green curve in Fig. 4. The functions changed are

$$U_{13}^{[1,2]}(R, \phi) = A_3 + D_3 e^{-b_3 R} + [B_3 e^{-\alpha(R-R_3)^2} + C_3 e^{-4\alpha(R-R_3)^2}](1 - \cos 2\phi) + E_3 e^{-\beta(R-R_4)^2} \sin^2 \phi \quad (2)$$

and

$$U_{13}^{[1]}(R, \phi) = B_2^{(13)} \exp[-\alpha_2^{(13)}(R-R_2^{(13)})^2] \sin 2\phi + (c_0^{(13)} + c_1^{(13)}R) \exp[-\alpha_4^{(13)}R] \sin 4\phi \quad (3)$$

where $A_3, B_3, C_3, D_3, E_3, R_3, R_4, b_3, \alpha, \beta, B_2^{(13)}, \alpha_2^{(13)}, R_2^{(13)}, c_0^{(13)}, c_1^{(13)}$, and

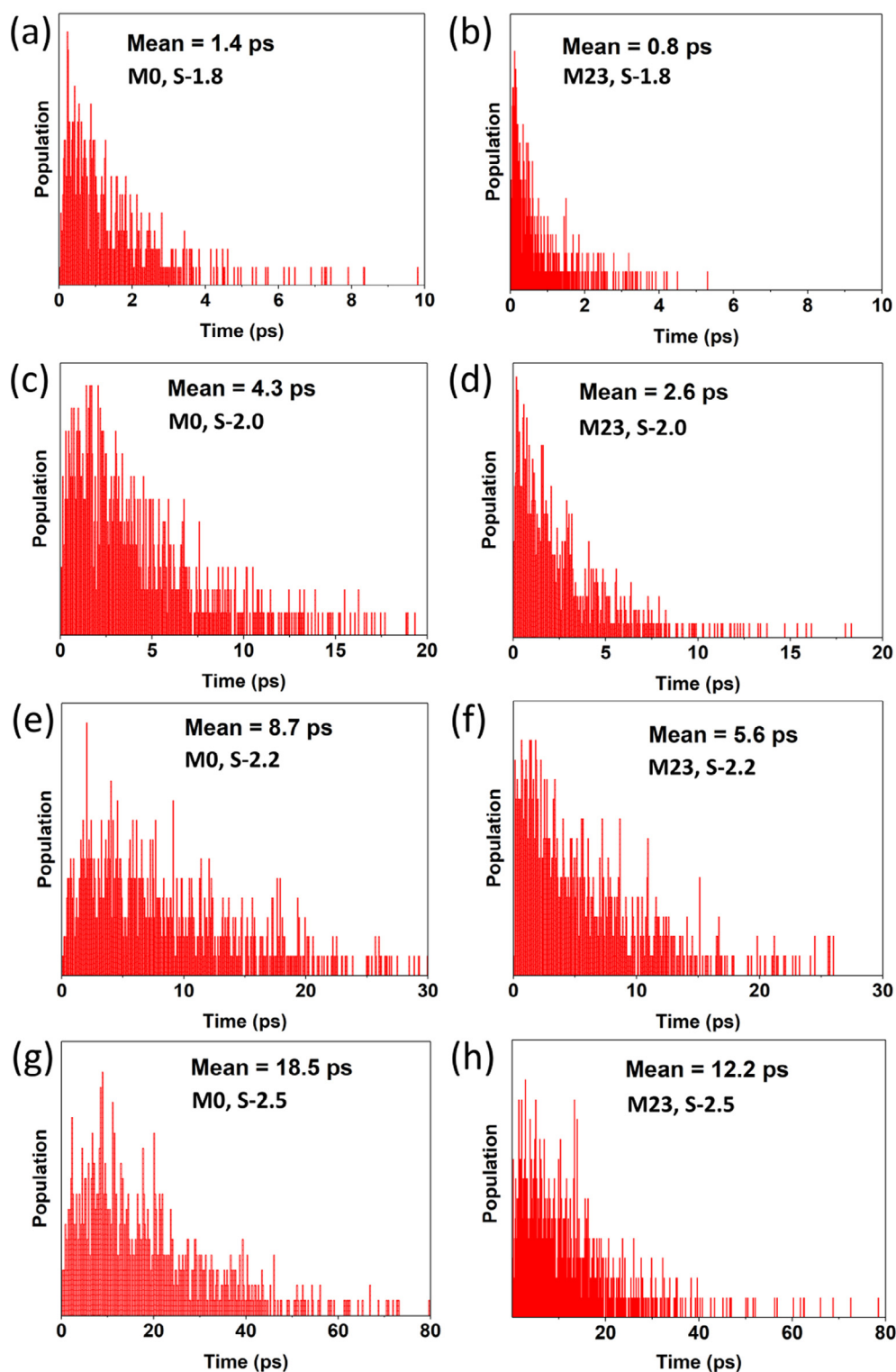


Fig. 6. (a) to (f), the histogram of the time of each trajectory hits the S_1 – S_2 CI region for M0 and M23 initial conditions for the S-1.8, S-2.0, S-2.2, S-2.5 PEMs.

$\alpha_4^{(13)}$ are parameters (explained in context in Ref. [45], but notice that the last term in Eq. (2) is added in the present work), and the changed parameters are in Tables 1 and 2. The fit is excellent; however, surface II degrades the behavior of the torsional potential for longer S-CH₃ bond distance as shown in Fig. 5.

Finally, to obtain reasonably good behavior at of the torsion potential for a range of S-CH₃ bond distances, we made PEM III by again re-fitting U_{33} and U_{13} . The parameters are again given in Tables 1 and

2, and the torsion potential for an equilibrium framework and equilibrium R is shown in purple in Fig. 4.

3. The shifted potential energy surfaces

In order to examine the role of the location and energy of the S_1 – S_2 crossing, we also made three shifted surfaces, each starting with PEM Ia. These PEMs were obtained by changing only the D_3 parameters in

Table 6
Average minimum of the adiabatic potential energy gap, $V(S_2) - V(S_1)$ in eV, along trajectories.^a

Surface set	M0	M23
I	0.36	0.25
S-1.8	0.28	0.21
S-2.0	0.19	0.20
S-2.5	0.13	0.13

^a Results for PEM I are from Ref. [45].

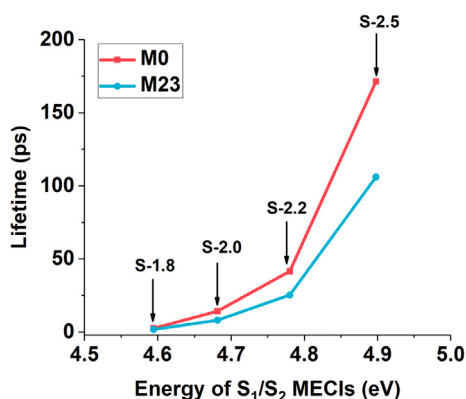


Fig. 7. The averaged photodissociation lifetime of the trajectories propagated on each of the shifted PESs, computed here as the average time to reach an S–C separation of 12 Å.

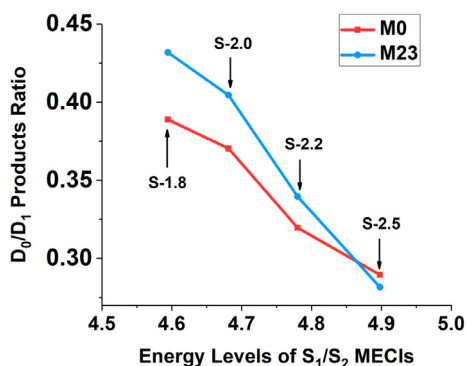


Fig. 8. The D_0/D_1 product ratio as a function of energy of the S_1/S_2 MECI.

equation (2). The shifted surfaces are denoted S-1.8, S-2.0, S-2.2, and S-2.5 to denote changing D_3 to 1.8, 2.0, 2.2, and 2.5 hartrees, respectively.

The minimum energy of the S_1 adiabatic surface is 4.36 eV at $R = 1.81$ Å, $\phi = 0$ (the same on all surfaces). To characterize the first conical intersection region (CI1 of Fig. 1), we optimized the S_1 – S_2 minimum-energy conical intersections (MECIs). The MECIs were optimized with CIOpt algorithm [64]. Table 3 shows the energies and R and ϕ coordinates of the optimized S_1 – S_2 MECIs. The table shows that the energies of the MECIs increase systematically as we shift the third diabatic state up, as shown in the schematic PESs in Fig. 2(a).

We also characterized the second conical intersection (CI2 of Fig. 1), and the results are in Table 4. We see that there is not much difference between the surfaces in this region, so our dynamical tests will be a test of the effect of varying the CI1 region.

4. Dynamics

4.1. Computational details of dynamics calculations and initial conditions

The nonadiabatic molecular dynamics is calculated with the

coherent switching with decay of mixing (CSDM) algorithm [65] implemented in the ANT software package [66]. The trajectories are carried out in the adiabatic representation, which is calculated on the fly from the fitted diabatic PEM that is being employed. All trajectories were terminated either after 0.5 ns or when the S–CH₃ distance exceeded 12 Å.

Two sets of initial conditions were studied; they are the same as in our previous dynamical study of this system and are explained in detail there [30] and so only summarized here. In brief, the first set of initial conditions is called M0 and is designed to approximately simulate photodissociation from the ground vibrational state of S_1 ; it has zero point energy in the S–C stretch (mode v_{23}) and seven other coupling-inducing vibrations, and it has 0.013 eV in each of the 34 other vibrational modes of S_1 . The second set of initial conditions is called M23 and is the same except that one quantum of vibrational excitation energy (0.086 eV) is added to v_{23} . The initial total energy for the M0 initial condition is 5.06 eV, and that for the M23 initial condition is 5.14 eV.

4.2. Dynamical role of the conical intersections

4.2.1. Lifetime of the photo-excited state

One thousand trajectories were calculated on each of the four shifted PEMs and with PEM III for each of the two sets of initial conditions. The lifetime of the photodissociation reaction is shown in Table 5. The table shows that the lifetime of the trajectories increases dramatically when we shift up the third diabatic state, as schematically shown in Fig. 2(a). The surface characteristics in Table 3 show that increasing the D_3 parameter moves the S_1 – S_2 MECI upward and outward, and the trajectory results in Table 5 show that this increases the lifetime. This is as we anticipated because it takes longer to accumulate the energy needed to access the conical intersection region when that region is higher in energy. To demonstrate this, we analyzed the first time that each trajectory hits the S_1 – S_2 CI region, which is identified here as the first time that the pointer state of CSDM algorithm is switched from the S_1 state to the S_2 state; this is shown as a histogram in Fig. 6. Notice that the abscissa range differs in each row of Fig. 6; the figure clearly shows that the average time of reaching the S_1 – S_2 CI region for the trajectories propagated on the four shifted PESs increases as we increase the D_3 parameter. In addition, the figure shows that the lifetimes of the trajectories for the M23 initial condition are much shorter than those for the M0 initial condition, which is due to the fact that the initial momentum along the S–CH₃ dissociation coordinate is larger for M23 initial condition than for the M0 initial condition. This is consistent with the previous conclusion in Ref. [14]. The lifetime of the photodissociation process for the S-2.5 PES and the M0 initial condition is 0.2 ns, still shorter than the experimental 1–2 ns [43,44], but closer than for the unshifted surfaces.

The trajectories do not pass precisely through the conical intersections because the conical intersections occur in a space with two less dimensions than the number of internal degrees of freedom. Nevertheless they do pass close to conical intersections. Table 6 gives some statistics for the average minimum of the energy gap along trajectories, and we see that it ranges from 0.13 to 0.28 eV. Although the trajectories do not actually access the conical intersection seams, the MECI does provide a surface descriptor that can be used to rationalize trends. Fig. 7 shows the average photodissociation lifetime of the trajectories propagated on the four shifted PESs as a function of the energy levels of the S_1 – S_2 MECIs for both M0 and M23 initial conditions. We see that the behavior of the lifetime as a function of the MECI energy level can be rationalized by in terms of S_1 – S_2 MECI energies as determining activation energies for accessing the seam region and hence for the photodissociation process occurring. By exciting the vibrational mode along the reaction coordinate, as in the M23 initial conditions, the energy to reach the activation barrier is pre-organized, resulting in a faster photodissociation rate for the M23 initial condition.

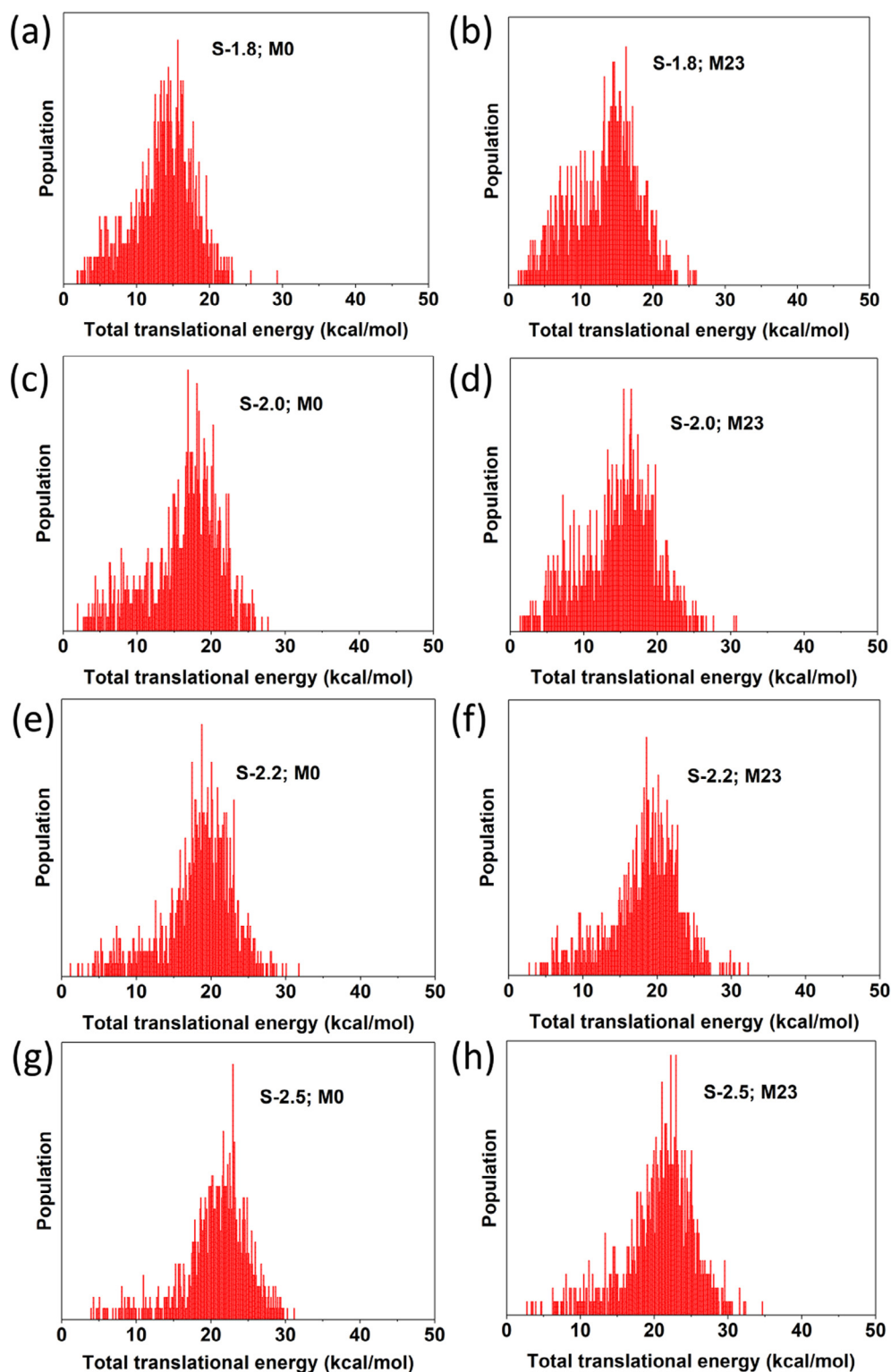


Fig. 9. (a) to (f), the histogram of the total translational energy for M0 and M23 initial conditions for the S-1.8, S-2.0, S-2.2, S-2.5 PESs.

It is especially worth emphasis that a small change in the MECI energy results in a large change of the dissociation lifetime; this underscores the importance of employing electronic structure calculations with quantitative accuracy. This is still a challenge for electronically nonadiabatic processes.

4.2.2. Mode specificity

Mode selectivity is observed experimentally in two ways: (1) By

exciting the S-CH₃ stretching mode, a dramatic increase of the D₀/D₁ product branching ratio was found. (2) The final translational energy distribution has different patterns with or without exciting the S-CH₃ stretching mode [22]. The computed D₀/D₁ ratios for the M0 initial condition, which corresponds to 0-0 excitation, are 0.39, 0.37, 0.32, 0.29, and 0.38 for the S-1.8, S-2.0, S-2.2, S-2.5 and III PEMs respectively. The D₀/D₁ ratios for the M23 initial conditions, which correspond to the initial condition of exciting the S-CH₃ stretch mode, are

0.43, 0.40, 0.34, 0.28 and 0.40 for the four shifted and III PEMs respectively. The relation between the D_0/D_1 product ratio and the energy levels of MECIs for the shifted PESs is shown in Fig. 8. Figure 8 shows that the D_0/D_1 products ratio decreases as we increase the energy level of the S_1 – S_2 MECIs. Although, we find product branching ratio mode selectivity for S-1.8, the branching ratio difference is still not comparable with experimental results. The experimental results have shown that the D_0/D_1 products ratio doubles by exciting the S–CH₃ stretching mode [22].

Next, we investigate the final total translational energy for the shifted PEMs. Figure 9 shows the total translation energy distributions for the two initial conditions of the four shifted PEMs. The mean values for M0 conditions are 13.6, 16.4, 18.3 and 20.8 kcal/mol for S-1.8, S-2.0, S-2.2 and S-2.5 PEMs. The mean values for M23 conditions are 13.3, 14.9, 18.3 and 20.7 kcal/mol for the four shifted PEMs. In the experiment, one peak around 16 kcal/mol for the 0–0 excitation and two peaks around 19 and 26 kcal/mol are found by exciting the S–CH₃ stretching mode [22]. However, the simulation results indicate that exciting the S–CH₃ stretching mode does not change the pattern or peak of total translational energy; instead, shifting the third diabatic state greatly shifts the peak of the total translational energy. This, to our understand, is because increasing the energy levels of S_1 – S_2 MECI, the trajectories require more energy along the S–CH₃ stretching direction to dissociate, and hence, with higher S_1 – S_2 MECI energy level, a larger total translational energy is found. However, there is no clear change of the translational pattern by exciting the S–CH₃ stretch mode.

5. Summarizing remarks

We have improved the three-state potential energy matrices for thioanisole in the following respects: (1) The ground-state torsional potential along ϕ has qualitatively improved behavior. (2) The diabatic coupling matrix element decays to exactly zero at the dissociation limit. (3) The third diabatic state is re-fitted such that it has better accuracy at $\phi = 0$. With these improvements, we have developed new versions of the potential energy surface PEM called II and III. In addition, to investigate the dynamical effect of the energy levels of S_2 – S_1 MECI, we have shifted the third diabatic state and generated shifted PEMs labeled S-1.8, S-2.0, S-2.2, and S-2.5.

By performing CSDM dynamical simulations using these PEMs, we are able to calculate photodissociation lifetimes much closer to the experimental ones than had been calculated with the original PEM. This is because shifting the energy level of the S_1 – S_2 MECI upwards means that the trajectories take more time to reach the strong interaction region. Shifting the energy level of S_1 – S_2 MECI by about 0.3 eV, the lifetime of the photodissociation process has increased by a factor of 69. This shows the importance of employing accurate electronic structure theory to obtain potential energy surfaces for dynamics simulations. In addition, we did find a little mode specificity for the S-1.8 PEM. By exciting the S–CH₃ stretching mode, the D_0/D_1 product branching ratio changes from 0.39 to 0.43, although this is still not as strong an effect as in the experimental results. We have also analyzed the total translational energy change when we shift the S_1 – S_2 MECI energy level. The peak of the total translational energy shifts to larger value when we shift the S_1 – S_2 MECI energy level up.

Acknowledgments

The authors are grateful to Shaohong Li for additional help, to Hua Guo and Changjian Xie for additional analysis of the PESs, and to Michael Ashfold for stimulating discussions of the dynamics. This work was supported in part by the U.S. Department of Energy, Office of Science, Office of Basic Energy Sciences under award number DE-

SC0015997.

References

- [1] P.J. Hay, R.T. Pack, R.B. Walker, E.J. Heller, *J. Phys. Chem.* 86 (1982) 862.
- [2] J. Biesner, L. Schnieder, J. Schmeer, G. Ahlers, X. Xie, K. Welge, M. Ashfold, R. Dixon, *J. Chem. Phys.* 88 (1988) 3607.
- [3] H. Guo, G.C. Schatz, *J. Chem. Phys.* 93 (1990) 393.
- [4] J.Z. Zhang, E.J. Heller, D. Huber, D.G. Imre, *J. Phys. Chem.* 95 (1991) 6129.
- [5] H. Guo, *J. Chem. Phys.* 96 (1992) 6629.
- [6] M.D. Person, P.W. Kash, L.J. Butler, *J. Chem. Phys.* 97 (1992) 355.
- [7] B. Heumann, K. Weide, R. Dürer, R. Schinke, *J. Chem. Phys.* 98 (1993) 5508.
- [8] E.E. Aubanel, J.-M. Gauthier, A.D. Bandrauk, *Phys. Rev. A* 48 (1993) 2145.
- [9] A.D. Hammerich, U. Manthe, R. Kosloff, H.-D. Meyer, L.S. Cederbaum, *Chem. Phys.* 101 (1994) 5523.
- [10] R.L. Miller, A.G. Suits, P.L. Houston, R. Toumi, J.A. Mack, A.M. Wodtke, *Science* 265 (1994) 1831.
- [11] J. Zhang, C.W. Riehn, M. Dulligan, C. Wittig, *J. Chem. Phys.* 103 (1995) 6815.
- [12] D.R. Yarkony, *J. Chem. Phys.* 104 (1996) 7866.
- [13] B.J. Greenblatt, M.T. Zanni, D.M. Neumark, *Science* 276 (1997) 1675.
- [14] D.A. Blank, W. Sun, A.G. Suits, Y.T. Lee, S.W. North, G.E. Hall, *J. Chem. Phys.* 108 (1998) 5414.
- [15] A. Talebpour, A.D. Bandrauk, K. Vijayalakshmi, S.L. Chin, *J. Phys. B* 33 (2000) 4615.
- [16] J.A. Davies, R.E. Continetti, D.W. Chandler, C.C. Hayden, *Phys. Rev. Lett.* 84 (2000) 5983.
- [17] A.L. Sobolewski, W. Domcke, *W. Eur. Phys. J. D* 20 (2002) 369.
- [18] G. Wu, B. Jiang, Q. Ran, J. Zhang, S.A. Harich, X. Yang, *J. Chem. Phys.* 120 (2004) 2193.
- [19] D.R. Yarkony, *J. Chem. Phys.* 121 (2004) 628.
- [20] M.L. Hause, Y.H. Yoon, F.F. Crim, *J. Chem. Phys.* 125 (2006) 174309.
- [21] M.L. Hause, Y.H. Yoon, A.S. Case, F.F. Crim, *J. Chem. Phys.* 128 (2008) 104307.
- [22] J.S. Lim, S.K. Kim, *Nat. Chem.* 2 (2010) 627.
- [23] R.N. Dixon, T.A.A. Oliver, M.N.R. Ashfold, *J. Chem. Phys.* 134 (2011) 194303.
- [24] J.H. Lehman, H. Li, J.M. Beames, M.L. Lester, *J. Chem. Phys.* 139 (2013) 141103.
- [25] X. Zhu, D.R. Yarkony, *J. Chem. Phys.* 140 (2014) 024112.
- [26] X. Xu, J. Zheng, K.R. Yang, D.G. Truhlar, *J. Am. Chem. Soc.* 136 (2014) 16378.
- [27] C. Xie, J. Ma, X. Zhu, D.H. Zhang, D.R. Yarkony, D. Xie, H. Guo, *J. Phys. Chem. Lett.* 5 (2014) 1055.
- [28] J. Krčmář, M.F. Gelin, W. Domcke, *J. Chem. Phys.* 143 (2015) 074308.
- [29] M. Epshtein, Y. Yifrach, A. Portnov, I. Bar, *J. Phys. Chem. Lett.* 7 (2016) 1717.
- [30] S.L. Li, D.G. Truhlar, *J. Chem. Phys.* 147 (2017) 044311.
- [31] K.C. Woo, D.H. Kang, S.K. Kim, *J. Am. Chem. Soc.* 139 (2017) 17152.
- [32] H. Köppel, W. Domcke, L.S. Cederbaum, *Adv. Chem. Phys.* 57 (1984) 59.
- [33] U. Manthe, H.-D. Meyer, L.S. Cederbaum, *J. Chem. Phys.* 97 (1992) 9062.
- [34] S.L. Mielke, G.J. Tawa, D.G. Truhlar, D.W. Schwenke, *J. Am. Chem. Soc.* 115 (1993) 6436.
- [35] D.R. Yarkony, *Rev. Mod. Phys.* 68 (1996) 985.
- [36] M.D. Hack, *J. Phys. Chem. A* 104 (2000) 8197.
- [37] G.A. Worth, L.S. Cederbaum, *Annu. Rev. Phys. Chem.* 55 (2004) 127.
- [38] A.W. Jasper, C. Zhu, S. Nangia, D.G. Truhlar, *Faraday Discuss.* 127 (2004) 1.
- [39] A.W. Jasper, S. Nangia, C. Zhu, D.G. Truhlar, *Acc. Chem. Res.* 39 (2006) 101.
- [40] B.G. Levine, T.J. Martínez, *Annu. Rev. Phys. Chem.* 58 (2007) 613.
- [41] G.A. Worth, H.-D. Meyer, H. Köppel, L.S. Cederbaum, I. Burghardt, *Int. Rev. Phys. Chem.* 27 (2008) 569.
- [42] Y. Shu, B.S. Fales, W.-T. Peng, B.G. Levine, *J. Phys. Chem. Lett.* 8 (2017) 4091.
- [43] M.N. Roberts, D.J. Hadden, L.T. Bergendahl, A.M. Wenge, S.J. Harris, T.N.V. Karsili, M.N.R. Ashfold, M.J. Peterson, V.G. Stavros, *Chem. Sci.* 4 (2013) 993.
- [44] M.H. Nagasaka, T. Suzuki, T. Ichimura, S. Kasahara, M. Baba, S. Kawauchi, *Phys. Chem. Chem. Phys.* 12 (2010) 13243.
- [45] S.L. Li, D.G. Truhlar, *J. Chem. Phys.* 146 (2017) 064301.
- [46] K.R. Yang, X. Xu, D.G. Truhlar, *J. Chem. Theory Comput.* 10 (2014) 924.
- [47] H. Nakamura, D.G. Truhlar, *J. Chem. Phys.* 118 (2003) 6816.
- [48] S.L. Li, D.G. Truhlar, M.W. Schmidt, M.S. Gordon, *J. Chem. Phys.* 142 (2015) 064106.
- [49] S.L. Li, X. Xu, C.E. Hoyer, D.G. Truhlar, *J. Phys. Chem. Lett.* 6 (2015) 3352.
- [50] H. Nakano, *J. Chem. Phys.* 99 (1993) 7983.
- [51] H. Nakano, *Chem. Phys. Lett.* 207 (1993) 372.
- [52] A.A. Granovsky, *J. Chem. Phys.* 134 (2011) 214113.
- [53] B.O. Roos, P.R. Taylor, P.E.M. Siegbahn, *Chem. Phys.* 48 (1980) 157.
- [54] K. Ruedenberg, M.W. Schmidt, M.M. Gilbert, S.T. Elbert, *Chem. Phys.* 71 (1982) 41.
- [55] Y. Zhao, D.G. Truhlar, *J. Chem. Theory Comput.* 4 (2008) 1849.
- [56] J.L. Bao, J. Zheng, D.G. Truhlar, *J. Am. Chem. Soc.* 138 (2016) 2690.
- [57] R. Krishnan, J.S. Binkley, R. Seeger, J.A. Pople, *J. Chem. Phys.* 72 (1980) 650.
- [58] T. Clark, J. Chandrasekhar, G.W. Spitznagel, P.V.R. Schleyer, *J. Comput. Chem.* 4 (1983) 294.
- [59] B.J. Lynch, Y. Zhao, D.G. Truhlar, *J. Phys. Chem. A* 107 (2003) 1384.
- [60] M.W. Schmidt, K.K. Baldridge, J.A. Boatz, S.T. Elbert, M.S. Gordon, J.H. Jensen, S. Koseki, N. Matsunaga, K.A. Nguyen, S.J. Su, T.L. Windus, M. Dupuis, J.A. Montgomery, *J. Comput. Chem.* 14 (1993) 1347.
- [61] M.S. Gordon, M.W. Schmidt, *Theory and Applications of Computational Chemistry: The First Forty Years*, Elsevier, Amsterdam, 2005, p. 1167.
- [62] L.A. Curtiss, K. Raghavachari, P.C. Redfern, V. Rassolov, J.A. Pople, *J. Chem. Phys.* 109 (1998) 7764.
- [63] P.L. Fast, M.L. Sanchez, D.G. Truhlar, *Chem. Phys. Lett.* 306 (1999) 407.
- [64] B.G. Levine, D.J. Coe, T.J. Martínez, *J. Phys. Chem. B* 112 (2008) 405.
- [65] C.Y. Zhu, S. Nangia, A.W. Jasper, D.G. Truhlar, *J. Chem. Phys.* 121 (2004) 7658.
- [66] J. Zheng, Z.-H. Li, A.W. Jasper, D.A. Bonhommeau, R. Valero, R. Meana-Pañeda, S.L. Mielke, D.G. Truhlar, ANT, version 2017, University of Minnesota, Minneapolis, 2017 <http://comp.chem.umn.edu/ant>.